Five-Component Decomposition Methods of Polarimetric SAR and Polarimetric SAR Interferometry Using Coupling Scattering Mechanisms

Yu Wang, *Student Member, IEEE*, Weidong Yu, *Member, IEEE*, and Wentao Hou

***Abstract*—In this article, five-component model-based decomposition methods of polarimetric synthetic aperture radar (PolSAR) (P5SD) and polarimetric synthetic aperture radar interferometry (PolInSAR) (PI5SD) using coupling scattering mechanisms are proposed. The target of these methods is to overcome the overestimation of volume scattering and to mitigate the mixed ambiguity of the scattering mechanism. First, coupling scattering models are proposed to decompose the coherency matrix into five submatrices. According to the traditional seven-component decomposition method proposed by Singh *et al.*, the helix and mixed dipole can be merged into a coupling component, while the oriented dipole and compound dipole can also be generated in a general form. Then, the refined volume scattering models of PolSAR are introduced to characterize the volume scattering power of various land covers. The polarimetric interferometric similarity parameter (PISP) is introduced to modify the refined volume scattering models, and it can be used to further reduce the volume scattering contribution of building areas with large orientation angles. In addition, a feature named θ_{dv}, total power, and PISP are embedded in the building area identification, and the building extraction results are used as the branch condition of the volume scattering model selection. In this article, the validity of P5SD and PI5SD can be demonstrated using airborne L-band E-SAR PolInSAR datasets and airborne C-band PolInSAR data collected by the Aerospace Information Research Institute, Chinese Academy of Sciences. The experimental results demonstrate that the P5SD and PI5SD can be used to effectively interpret the scattering characteristics of the ambiguous regions.**

***Index Terms*—Coupling scattering, five-component decomposition, overestimation of volume scattering (OVS), polarimetric synthetic aperture radar (PolSAR), polarimetric synthetic aperture radar interferometry (PolInSAR).**

Manuscript received November 25, 2020; revised March 13, 2021; accepted March 27, 2021. Date of publication April 6, 2021; date of current version July 14, 2021. This work was supported in part by the National Key Research and Development Program of China under Grant 2017YFB0502700 and in part by the Beijing Natural Science Foundation under Grant 4192065. *(Corresponding author: Wentao Hou.)*

The authors are with the Department of Space Microwave Remote Sensing System, Aerospace Information Research Institute, Chinese Academy of Sciences, Beijing 100190, China, and also with the School of Electronic, Electrical and Communication Engineering, University of Chinese Academy of Sciences, Beijing 100039, China (e-mail: wangyu370705@163.com; ywd@mail.ie.ac.cn; houwentao17@mails.ucas.edu.cn.).

Digital Object Identifier 10.1109/JSTARS.2021.3071161

I. Introduction

With the development of the synthetic aperture radar (SAR) imaging and measurement techniques, polarimetric SAR (PolSAR), as an important branch of SAR application, is widely used in many fields. Among the applications of PolSAR, polarimetric decomposition is a useful way to interpret the complete electromagnetic scattering information, and it plays an important role in characterizing the scattering mechanism of various terrain types. The incoherent decomposition techniques can be divided into two main categories, including eigenvalue-based decomposition [1], [2] and model-based decomposition [3]–[11]. In the model-based decomposition method, a coherency matrix can be decomposed into the weighted sum of several scattering models with clearer physical nature. These scattering models can be used to interpret the scattering mechanism of various land covers. The most important shortcomings of the model-based decomposition methods are the overestimation of volume scattering (OVS) and the negative scattering powers. According to these shortcomings, a large number of excellent decomposition methods have been proposed to overcome the OVS and reduce the number of negative power pixels [1]–[11]. These decomposition methods have been widely applied to glacier monitoring [12]–[14], soil moisture retrieval [15]–[18], and disaster assessment [19], [20].

The most famous model-based decomposition method is the three-component decomposition method (FDD) proposed by Freeman and Durden [3]. Although this method is simple and easy for implementation, the OVS caused by the assumption of reflection symmetry occurs. Yamaguchi *et al.* [4] added the helix scattering component, which was introduced by Huynen through mathematical derivation [18], into the decomposition method (Y4O). Y4O considers the imaginary of T_{23} and reduces the proportion of volume scattering component. Based on the Y4O, orientation angle compensation (OAC) was employed by Yamaguchi *et al.* [6], and the four-component decomposition method with rotation matrix (Y4R) was obtained. The volume scattering power can be further reduced via the Y4R. Based on the Y4R, Sato *et al.* [8] decomposed the scattering mechanisms of various land covers with extended volume scattering model (S4R) and obtained better decomposition results. To depict the scattering mechanism of various terrain types, Zhang *et al.* [5]

added the wire scattering component to the analysis of PolSAR images, and the method (MCSM) is effective for analysis of buildings in urban areas. Then, MCSM was further extended by Xiang *et al.* [21], and this extended method can be abbreviated as MCSMs. In 2013, the phase angle compensation proposed by Singh *et al.* [9] was employed in the Y4R, and the general four-component decomposition method (G4U) was proposed to overcome the OVS. In this case, the scattering mechanism of urban area can be characterized. Based on the G4U, an extended method using the ratio of correlation coefficient was proposed by Quan *et al.* [22], which can be abbreviated as ExG4URcc. The method can be used to characterize the scattering mechanisms of various land covers. In 2015, Xiang *et al.* proposed the cross-scattering component, in which the building orientation angle is considered. This method can be used to separate the cross scattering of urban areas from the overall HV component. In aforementioned decomposition methods, since the cross- and co-polarization are considered to be uncorrelated, the T_{13} and T_{23} terms are forced to zero. However, PolSAR data cannot always satisfy this assumption, and the polarimetric information cannot be fully utilized. In addition to the vegetation areas, the oriented buildings also contribute to the cross-pol HV scattering, thereby leading to substantial volume scattering. According to the deficiencies of the assumption of reflection symmetry, Singh and Yamaguchi [10] proposed a six-component decomposition method (6SD), which considers oriented dipoles and compound scattering components. The decomposition results obtained via this method are consistent with the terrain types, including ocean, forests, and orthogonal buildings. The volume scattering of the buildings with large orientation angles can be effectively reduced.

For the building areas orthogonal to the radar line of sight (LOS), the scattering mechanism can be effectively characterized without any rotation. When the rotation angle between the vertical wall of the oriented building and the flight direction is small, the OAC can effectively reduce the cross-pol power by minimizing the term T_{33} in the coherency matrix. However, when the rotation angle between the vertical wall of the oriented building and the direction of flight exceeds a specified range, the OAC is no longer effective, and the oriented building induces a strong cross-pol power contribution [23], [24]. Chen *et al.* [23] found that there is still a strong volume scattering contribution after OAC. Deng and Yan [25] pointed out that the volume scattering of the forest canopy is not only induced by the terrain slopes, but also induced by the randomly oriented cylinder-like scatterers. Therefore, although the OAC can be used to rotate oriented buildings to the LOS, it is effective only within a certain range of rotation angle. When the oriented angle is beyond this range, the OAC may cause serious problems.

To evaluate the efficiency of the OAC, the OAC has been extensively investigated [26], [27]. Lee *et al.* [27] derived the relationship between OAC and terrain slopes, and the derived OAC has robust physical meaning. Although the OAC can be used to reduce the number of negative pixels by reducing the value of T_{33} element to less than that of T_{22}, the T_{33} value of pixels with large T_{33} values in the forests will be mistakenly reduced [28]. In addition, when the orientation angles of buildings exceed a certain range, the OAC will no longer be effective [29].

To avoid the errors induced by the OAC operation, Singh *et al.* [11] proposed a seven-component decomposition method (7SD) by employing mixed dipoles into the 6SD. In this method, all elements of the coherency matrix can be considered. The rotation of the coherency matrix is not required by the 7SD, and the original data matrix can be preserved. Although the models can illustrate the real and imaginary parts of T_{13} and T_{23} mathematically, the physical meanings corresponding to these models are not clear. Since T_{13} and T_{23} are the Pauli-based coupling terms, two coupling scattering components are proposed in this article to characterize the physical meanings of these coupling terms. If the cross- and co-polarization are irrelevant, these coupling terms are forced to zero; otherwise, these coupling models can be used to reflect the coupling information.

In recent decades, by improving volume scattering models and employing auxiliary mathematical tools, many methods with improved volume scattering models [9], [22], [30] and extended scattering components [5], [21], [31] have been proposed to overcome the OVS and negative scattering powers. Although the improved volume scattering models were demonstrated to be effective for the inevitable defects and can be used to substantially enhance the decomposition performance, the methods are limited by the computational efficiency due to the additional parameters. In this article, refined volume scattering models are proposed to characterize the mechanism of various land covers without extra computation. Full deorientation could be applied to the coherency matrix by placing the orientation angles into the probability density functions, and these refined probability density functions minimize the HV scattering component of the coherency matrix. The refined volume scattering models are related to the orientation angles. By selecting various volume scattering models, the scattering characteristics of various terrain types with different orientation angles can be reasonably characterized to avoid ambiguity of the scattering mechanism.

In the polarimetric SAR interferometry (PolInSAR) image data, target decomposition is one of the most effective applications [32]–[34]. PolInSAR, which combines interferometric and polarimetric information, not only successfully interprets the characteristics of the targets, but also distinguishes oriented buildings from the vegetation areas. Polarimetric interferometric similarity parameter (PISP) is an important parameter associated with the physical properties of various targets and is polarimetric dependent [33], [34]. The PISP magnitude in the forest areas is lower than that in the built-up areas that contain more permanent scatterers, and PolInSAR coherence has close relationship with the forest types and structures [35]. Therefore, the coherence parameter can be used to model the volume scattering. In this article, the PISP is used to modify the refined volume scattering models to further reduce the volume scattering power of buildings with large orientation angles.

In this article, model-based five-component decomposition methods of PolSAR (P5SD) and PolInSAR (PI5SD) using coupling scattering components are proposed to overcome the OVS. Specific mathematical derivations of the refined volume scattering models are derived from [36], and these refined

volume scattering models are further modified using the PISP so that these refined volume scattering models are suitable for PolInSAR data. Comparisons are carried out to demonstrate the superiority of the P5SD and PI5SD in overcoming the OVS. The performance of the P5SD and PI5SD is evaluated using airborne L-band E-SAR PolInSAR data and airborne C-band PolInSAR data collected by the Aerospace Information Research Institute (AIR), Chinese Academy of Sciences.

II. Methodology

PolSAR acquires the polarimetric scattering matrix of each pixel in the scene by transmitting and receiving electromagnetic waves of different polarization modes, so as to analyze the target scattering characteristics. The general form of the radar scattering matrix is

$$[S] = \begin{bmatrix} S_{\mathrm{HH}} & S_{\mathrm{HV}} \\ S_{\mathrm{VH}} & S_{\mathrm{VV}} \end{bmatrix} \tag{1}$$

where S_{HH}, S_{HV}, S_{VH}, and S_{VV} are the complex elements of the scattering matrix. $S_{\mathrm{HV}} = S_{\mathrm{VH}}$, which is consistent with the reciprocity assumption. S_{VH} is the backscattered return from horizontal transmitting and vertical receiving polarization.

For the case of monostatic backscattering, samples are averaged to form the coherency matrix. The corresponding coherency matrix is written as

$$\begin{aligned} \langle [\mathbf{T}] \rangle = \left\langle k_p k_p^{\dagger} \right\rangle &= \begin{bmatrix} T_{11} & T_{12} & T_{13} \\ T_{21} & T_{22} & T_{23} \\ T_{31} & T_{32} & T_{33} \end{bmatrix} \\ &= \begin{bmatrix} \left\langle |k_1|^2 \right\rangle & \langle k_1 k_2^* \rangle & \langle k_1 k_3^* \rangle \\ \langle k_2 k_1^* \rangle & \left\langle |k_2|^2 \right\rangle & \langle k_2 k_3^* \rangle \\ \langle k_3 k_1^* \rangle & \langle k_3 k_2^* \rangle & \left\langle |k_3|^2 \right\rangle \end{bmatrix} \end{aligned} \tag{2}$$

where

$$k_p = \begin{bmatrix} k_1 \\ k_2 \\ k_3 \end{bmatrix} = \frac{1}{\sqrt{2}} \begin{bmatrix} S_{\mathrm{HH}} + S_{\mathrm{VV}} \\ S_{\mathrm{HH}} - S_{\mathrm{VV}} \\ 2S_{\mathrm{HV}} \end{bmatrix}. \tag{3}$$

A. Compound Scattering Matrix

The scattering matrix contains complete polarimetric backscattering information and is related to the shape, orientation, material, and other factors of the target parameters. Within a radar range, if a single target exists, the scattering matrix is uniquely determined by the point target; if there are multiple targets within a radar range, the compounded matrix is composed of scattering matrices of multiple targets [21]. However, there are usually multiple targets in the same radar range, and the compound scattering theory is universally used.

According to the theory proposed by Kitayama *et al.* [36], if the distance between two or more targets is less than the radar range resolution, the compounded matrix composed of multiple targets in the range resolution can be expressed as a weighted sum of multiple scattering matrices. Considering the condition where there are two targets with a distance d in the resolution unit, the compound scattering matrix can be expressed as

$$\begin{aligned} [S]^{\mathrm{total}} &= [S]_1 + [S]_2 P(d) = [S]_1 + [S]_2 \exp\left(-j\tfrac{4\pi d}{\lambda}\right) \\ &= [S]_1 + [S]_2 \exp\left(-j\theta\right) \end{aligned} \tag{4}$$

where $P(d) = \exp(-j\frac{4\pi d}{\lambda}) = \exp(-j\theta)$ denotes the phase delay caused by the spatial distance d. When d is 0, $\lambda/8$, and $\lambda/4$, $P(d)$ is

$$P(0) = 1, P\left(\frac{\lambda}{8}\right) = -j, P\left(\frac{\lambda}{4}\right) = -1 \tag{5}$$

where

$$\begin{cases} d = 0 \Rightarrow \theta = 0 \\ d = \lambda/8 \Rightarrow \theta = \pi/2 \\ d = \lambda/4 \Rightarrow \theta = \pi. \end{cases} \tag{6}$$

The scattering characteristics of various objects can be regarded as the composition of dipoles with different orientation angles [10]. The configurations of the scattering mechanisms can be derived using the dipoles with various orientation angles. In this case, the reasonable scattering models corresponding to the scattering mechanisms can be obtained to characterize the composition of the scattering mechanisms of various land covers.

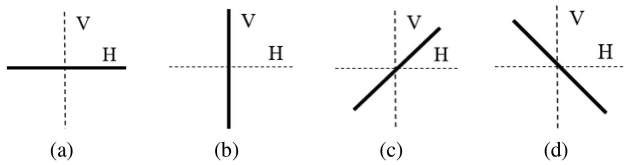

Fig. 1. Configurations of dipoles. (a) Horizontal dipole. (b) Vertical dipole. (c) 45° oriented dipole. (d) -45° oriented dipole.

According to the configurations shown in Fig. 1(a) and (b), the scattering matrices of horizontal and vertical dipoles can be written as

$$[S]^{\mathrm{H}}_{\mathrm{dipole}} = \begin{bmatrix} 1 & 0 \\ 0 & 0 \end{bmatrix}, [S]^{\mathrm{V}}_{\mathrm{dipole}} = \begin{bmatrix} 0 & 0 \\ 0 & 1 \end{bmatrix} \tag{7}$$

where the superscripts "H" and "V" denote horizontal and vertical directions, respectively. The scattering matrices of dipoles with $\pm 45^\circ$ orientation angles [shown in Fig. 1(c) and (d)] can be written as

$$\begin{aligned} [S]^{45^\circ}_{\mathrm{dipole}} &= [S]_1 = \frac{1}{2} \begin{bmatrix} 1 & 1 \\ 1 & 1 \end{bmatrix} \\ [S]^{-45^\circ}_{\mathrm{dipole}} &= [S]_2 = \frac{1}{2} \begin{bmatrix} 1 & -1 \\ -1 & 1 \end{bmatrix}. \end{aligned} \tag{8}$$

According to the 6SD proposed by Singh and Yamaguchi [10], the surface and dihedral scattering matrices can be written as follows:

Dihedral scattering:

$$[S]^{\mathrm{total}}_{\mathrm{dihedral}} = [S]^{\mathrm{H}}_{\mathrm{dipole}} + [S]^{\mathrm{V}}_{\mathrm{dipole}} \exp\left(-j\pi\right) = \begin{bmatrix} 1 & 0 \\ 0 & -1 \end{bmatrix} \tag{9}$$

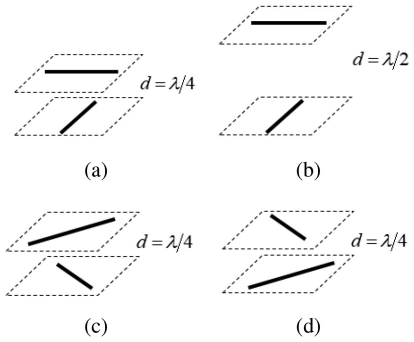

Fig. 2. Configurations of scattering models. (a) Dihedral. (b) Surface. (c) Right rotated dihedral. (d) Left rotated dihedral.

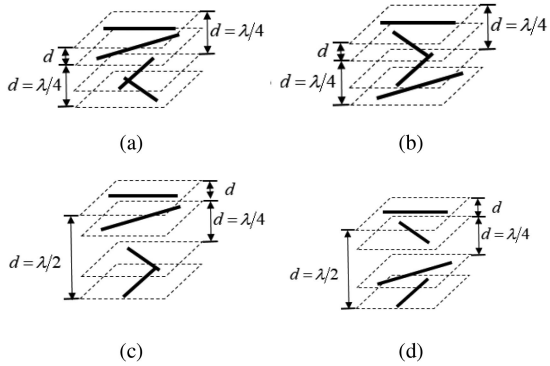

Fig. 3. Configurations of coupling matrices. (a) Dihedral and right rotated dihedral offset by d. (b) Dihedral and left rotated dihedral offset by d. (c) Surface and right-rotated dihedral offset by d. (d) Surface and left-rotated dihedral offset by d.

Surface scattering:

$$[S]^{\text{total}}_{\text{surface}} = [S]^{\text{H}}_{\text{dipole}} + [S]^{\text{V}}_{\text{dipole}} \exp(-j2\pi) = \begin{bmatrix} 1 & 0 \\ 0 & 1 \end{bmatrix}. \quad (10)$$

In this article, the configuration of the surface scattering mechanism is modified. To eliminate the errors caused by one of the two dipoles having a slight distance from the plane (shown in [10]), the horizontal and vertical dipoles are placed at two different planes with an offset distance of $\frac{\lambda}{2}$, as shown in Fig. 2(b).

The corresponding coherency matrices of the surface and double-bounce scattering components are further modified as

$$[T]_{\text{s}} = \frac{1}{1+|\beta|^2} \begin{bmatrix} 1 & \beta^* & 0 \\ \beta & |\beta|^2 & 0 \\ 0 & 0 & 0 \end{bmatrix}$$
$$[T]_{\text{d}} = \frac{1}{1+|\alpha|^2} \begin{bmatrix} |\alpha|^2 & \alpha & 0 \\ \alpha^* & 1 & 0 \\ 0 & 0 & 0 \end{bmatrix} \quad (11)$$

where α and β are the shape parameters of double-bounce and surface scattering, respectively.

The volume scattering models can be obtained using the dipoles with $\pm 45^\circ$ orientation angles. The right- and left-rotated volume scattering models are shown in Fig. 2(c) and (d), respectively. The 45°- and -45°-oriented dipoles are placed in two planes with an offset distance of quarter-wave, and the scattering matrices can be expressed as

$$[S]^{45^\circ}_{\text{v}} = [S]^{45^\circ}_{\text{dipole}} + [S]^{-45^\circ}_{\text{dipole}} \exp(-j\pi) = \begin{bmatrix} 0 & 1 \\ 1 & 0 \end{bmatrix} \quad (12)$$

$$[S]^{-45^\circ}_{\text{v}} = [S]^{-45^\circ}_{\text{dipole}} + [S]^{45^\circ}_{\text{dipole}} \exp(-j\pi) = \begin{bmatrix} 0 & -1 \\ -1 & 0 \end{bmatrix}. \quad (13)$$

According to Fig. 2, the volume scattering models can be obtained by rotating the dihedral scattering model by $45^\circ/-45^\circ$. The phenomenon demonstrates that when the orientation angle reaches $\pm 45^\circ$, the dominant scattering of the regions where the dominant scattering mechanism is double-bounce scattering will be mistakenly recognized as the volume scattering, resulting in the OVS. In this case, the traditional volume scattering models are not suitable for the ground truth. In this article, refined volume scattering models of PolSAR, corresponding to [37], are introduced to characterize the scattering mechanisms of various land covers.

According to the definition of coherency matrix elements, terms T_{13} and T_{23} are regarded as the coupling terms between the first/second and third Pauli scattering vectors. By extending the Gulab's model [11] into a general way, the coupling model of T_{13} is composed of a surface scattering model and a volume scattering model with an offset d. In this coupling model, the offset value d is variable, and it depends on the orientation angle of the T_{13} element, namely, θ_{sv}. The scattering matrices [shown in Fig. 3(a) and (b)] of T_{13} can be separately written as

$$[S]^{r}_{\text{sv}} = [S]^{\text{total}}_{\text{surface}} + [S]^{45^\circ}_{\text{v}} \exp(-j\theta_{\text{sv}}) = \begin{bmatrix} 1 & \exp(-j\theta_{\text{sv}}) \\ \exp(-j\theta_{\text{sv}}) & 1 \end{bmatrix} \quad (14)$$

$$[S]^{l}_{\text{sv}} = [S]^{\text{total}}_{\text{surface}} + [S]^{-45^\circ}_{\text{v}} \exp(-j\theta_{\text{sv}}) = \begin{bmatrix} 1 & -\exp(-j\theta_{\text{sv}}) \\ -\exp(-j\theta_{\text{sv}}) & 1 \end{bmatrix} = \begin{bmatrix} 1 & \exp[-j(\theta_{\text{sv}}+\pi)] \\ \exp[-j(\theta_{\text{sv}}+\pi)] & 1 \end{bmatrix} \quad (15)$$

where the subscript "sv" denotes the coupling term of surface and volume scattering models. Two previously described compound scattering models can be merged into a general form, and the scattering model can be written as

$$[S]^{\text{total}}_{\text{sv}} = [S]^{\text{total}}_{\text{surface}} + [S]^{-45^\circ}_{\text{v}} \exp(-j\theta) = \begin{bmatrix} 1 & \exp(-j\theta_{\text{sv}}) \\ \exp(-j\theta_{\text{sv}}) & 1 \end{bmatrix}, \quad \theta_{\text{sv}} \in [0, 2\pi]. \quad (16)$$

According to the mathematical relationship between the scattering matrix and the coherency matrix, the coherency matrix of

T_{13} term can be expressed as

$$[T]_{\mathrm{sv}} = \frac{1}{2}\begin{bmatrix} 1 & 0 & \exp(j\theta_{\mathrm{sv}}) \\ 0 & 0 & 0 \\ \exp(-j\theta_{\mathrm{sv}}) & 0 & 1 \end{bmatrix}, \quad \theta_{\mathrm{sv}} \in [0, 2\pi]. \tag{17}$$

Similarly, the scattering matrices [shown in Fig. 3(c) and (d)] of T_{23} can be written as

$$\begin{aligned}[S]_{\mathrm{dv}}^{r} &= [S]_{\mathrm{dihedral}}^{\mathrm{total}} + [S]_{\mathrm{v}}^{45^\circ}\exp(-j\theta_{\mathrm{dv}}) \\ &= \begin{bmatrix} 1 & \exp(-j\theta_{\mathrm{dv}}) \\ \exp(-j\theta_{\mathrm{dv}}) & -1 \end{bmatrix}\end{aligned} \tag{18}$$

$$\begin{aligned}[S]_{\mathrm{dv}}^{l} &= [S]_{\mathrm{dihedral}}^{\mathrm{total}} + [S]_{\mathrm{v}}^{-45^\circ}\exp(-j\theta_{\mathrm{dv}}) \\ &= \begin{bmatrix} 1 & \exp[-j(\theta_{\mathrm{dv}}+\pi)] \\ \exp[-j(\theta_{\mathrm{dv}}+\pi)] & -1 \end{bmatrix}.\end{aligned} \tag{19}$$

The general form of the compound scattering matrix can be derived as

$$\begin{aligned}[S]_{\mathrm{dv}}^{\mathrm{total}} &= [S]_{\mathrm{surface}}^{\mathrm{total}} + [S]_{\mathrm{v}}^{-45^\circ}\exp(-j\theta_{\mathrm{dv}}) \\ &= \begin{bmatrix} 1 & \exp(-j\theta_{\mathrm{dv}}) \\ \exp(-j\theta_{\mathrm{dv}}) & -1 \end{bmatrix}, \quad \theta_{\mathrm{dv}} \in [0, 2\pi].\end{aligned} \tag{20}$$

The corresponding coherency matrix of the T_{23} term can be expressed as

$$[T]_{\mathrm{dv}} = \frac{1}{2}\begin{bmatrix} 0 & 0 & 0 \\ 0 & 1 & \exp(j\theta_{\mathrm{dv}}) \\ 0 & \exp(-j\theta_{\mathrm{dv}}) & 1 \end{bmatrix}, \quad \theta_{\mathrm{dv}} \in [0, 2\pi]. \tag{21}$$

In the above equations, θ_{sv} and θ_{dv} are used to characterize the offset distance between scattering models, which are written as

$$\theta_{\mathrm{sv}} = \mathrm{angle}(T_{13}), \quad \theta_{\mathrm{dv}} = \mathrm{angle}(T_{23}). \tag{22}$$

B. Modification of PolInSAR Volume Scattering Models

For the PolInSAR system, polarimetric interferometric information can be described by a 6×6 coherency matrix $\langle \mathbf{T}_6 \rangle$, which is defined as

$$\langle \mathbf{T}_6 \rangle = \left\langle \begin{bmatrix} k_1 \\ k_2 \end{bmatrix} \begin{bmatrix} k_1^{\mathrm{H}} & k_2^{\mathrm{H}} \end{bmatrix} \right\rangle = \begin{bmatrix} \langle T_{11} \rangle & \langle \Omega_{12} \rangle \\ \langle \Omega_{21} \rangle & \langle T_{22} \rangle \end{bmatrix} \tag{23}$$

where "H" denotes the complex conjugate transpose and k_1 and k_2 are the scattering vectors for an interferometric pair. $\langle T_{11} \rangle$ and $\langle T_{22} \rangle$ are the Hermite matrices for master and slave polarimetric images, respectively, and $\langle \Omega_{12} \rangle$ is the non-Hermite matrix containing polarimetric and interferometric information.

The interferometric coherence coefficient and phase information have a strong dependence on the polarization state. According to the theory of polarization coherence coefficients [38], by projecting Pauli-based scattering vectors k_1 and k_2 onto the unit projection vectors ω_1 and ω_2, the PISP can be obtained. The unit projection vectors correspond to the polarization scattering system. The specific expression of the optimal parameter PISP is derived from [34].

According to [34], the PISP is independent of the absolute amplitude information of the scattering matrix and the orientation angle of the target and can be used to characterize the polarization interference stability information of various ground targets. As a second-order statistical parameter of PolInSAR, the PISP can be used to effectively describe the characteristics of ground scattering. The higher the stability of the target, the larger the value of the PISP. Since the scattering mechanism in the building area is deterministic and the scattering mechanism in the forest area is stochastic, the PISP value in the building area is relatively large, while the PISP value in the forest area is relatively small. In this case, the PISP can be used to reduce the T_{33} term of the coherency matrix of volume scattering so that the volume scattering contribution of building areas with large orientation angles can be reasonably reduced

$$\langle [T] \rangle_{v\_\mathrm{new}} = \begin{bmatrix} T_{v11} & T_{v12} & T_{v13} \\ T_{v21} & T_{v22} & T_{v23} \\ T_{v31} & T_{v32} & rrT_{v33} \end{bmatrix} \tag{24}$$

where $rr = \frac{\mathrm{PISP}}{(1-\mathrm{PISP})}$ and $T_{vij}(i, j = 1, 2, 3)$ is the element in the ith row and the jth column of the coherency matrix of volume scattering. Since $\frac{d(rr)}{d(\mathrm{PISP})} = \frac{1}{(1-\mathrm{PISP})^2} > 0$, rr is an incremental function of the PISP, which can be adaptively changed in the volume scattering model. When $rr \leq 1$, the scattering mechanism of this region is stochastic, and the volume scattering models are the same as that in [37]. When $rr > 1$, the scattering mechanism of this region is deterministic, and the modified volume scattering models obtained via (24) are used for the decomposition.

C. Decomposition Methods of PolSAR and PolInSAR Data

Using the refined volume scattering corresponding to [37] and the proposed coupling scattering components, the P5SD and PI5SD can be proposed to evaluate the performance of the new scattering models, and the coherency matrix can be divided into

$$\begin{aligned}\langle [T] \rangle &= f_{\mathrm{s}}[T]_{\mathrm{s}} + f_{\mathrm{d}}[T]_{\mathrm{d}} + f_{\mathrm{sv}}[T]_{\mathrm{sv}} + f_{\mathrm{dv}}[T]_{\mathrm{dv}} \\ &+ f_{\mathrm{v}} \begin{cases} \langle [T] \rangle_{v}^{i} \, (\mathrm{PolSAR-Data}) \\ \langle [T] \rangle_{v\_new}^{i} \, (\mathrm{PolInSAR-Data}) \end{cases}\end{aligned} \tag{25}$$

where f_{s}, f_{d}, f_{sv}, f_{dv}, and f_{v} are coefficients to be determined. $[T]_{\mathrm{s}}$ and $[T]_{\mathrm{d}}$ are the models corresponding to surface and double-bounce scattering, respectively. $[T]_{\mathrm{sv}}$ and $[T]_{\mathrm{dv}}$ are the models corresponding to the coupling scattering introduced in this article. $\langle [T] \rangle_{v}^{i}$ and $\langle [T] \rangle_{v\_\mathrm{new}}^{i}$ $(i = 1, 2, 3, 4)$ are the refined volume scattering model of PolSAR and PolInSAR, respectively, and different values of i correspond to different refined volume scattering models.

In this article, the PolInSAR data are selected to derive the representations of the coefficients and their relationships.

1) Sinusoidal Distribution: If $\langle[T]\rangle^1_{v\_\text{new}}$ is selected as the coherency matrix corresponding to volume scattering, the elements relations can be written as

$$\begin{aligned}
T_{11} &= f_\text{s} + f_\text{d}|\alpha|^2 + \frac{f_\text{v}}{2} + \frac{f_\text{sv}}{2} \\
T_{12} &= f_\text{s}\beta^* + f_\text{d}\alpha + \frac{f_\text{v}\cos 2\theta_\text{d}}{6} \\
T_{13} &= \frac{f_\text{sv}}{2}\exp\left(-j\theta_\text{sv}\right) \\
T_{22} &= f_\text{s}|\beta|^2 + f_\text{d} + \frac{f_\text{dv}}{2} + \frac{\left(15-\cos 4\theta_\text{d}\right)f_\text{v}}{60} \\
T_{23} &= \frac{f_\text{dv}}{2}\exp\left(-j\theta_\text{dv}\right) \\
T_{33} &= \frac{rr\left(15+\cos 4\theta_\text{d}\right)f_\text{v}}{45-\cos 4\theta_\text{d}+rr\left(15+\cos 4\theta_\text{d}\right)} + \frac{f_\text{dv}}{2} + \frac{f_\text{sv}}{2}.
\end{aligned} \tag{26}$$

According to (26), the values of f_sv, f_dv, and f_v can be derived directly. Once f_sv, f_dv, and f_v have been determined, three equations with four unknowns (α, β, f_s, and f_d) can be defined

$$\begin{aligned}
&f_\text{dv} = 2abs\left(T_{23}\right), f_\text{sv} = 2abs\left(T_{13}\right) \\
&f_\text{v} = \left[\frac{45-\cos 4\theta_\text{d}}{2rr\left(15+\cos 4\theta_\text{d}\right)} + \frac{1}{2}\right]\left(2T_{33} - f_\text{sv} - f_\text{dv}\right) \\
&S = f_\text{s} + f_\text{d}|\alpha|^2 = T_{11} - \frac{f_\text{v}}{2} - \frac{f_\text{sv}}{2} \\
&C = f_\text{s}\beta^* + f_\text{d}\alpha = T_{12} - \frac{f_\text{v}\cos 2\theta_\text{d}}{6} \\
&D = f_\text{s}|\beta|^2 + f_\text{d} = T_{22} - \frac{f_\text{dv}}{2} - \frac{\left(15-\cos 4\theta_\text{d}\right)f_\text{v}}{60}.
\end{aligned} \tag{27}$$

2) Uniform Distribution: Similarly, when the uniform distribution is selected, the coefficients and their relationships are expressed as

$$\begin{aligned}
&f_\text{dv} = 2abs\left(T_{23}\right), f_\text{sv} = 2abs\left(T_{13}\right) \\
&f_\text{v} = \left(\frac{1}{2} + \frac{3}{2rr}\right)\left(2T_{33} - f_\text{sv} - f_\text{dv}\right) \\
&S = f_\text{s} + f_\text{d}|\alpha|^2 = T_{11} - \frac{f_\text{v}}{2} - \frac{f_\text{sv}}{2} \\
&C = f_\text{s}\beta^* + f_\text{d}\alpha = T_{12} \\
&D = f_\text{s}|\beta|^2 + f_\text{d} = T_{22} - \frac{f_\text{dv}}{2} - \frac{f_v}{4}.
\end{aligned} \tag{28}$$

3) Cosine Distribution: In this case, $\langle[T]\rangle^3_{v\_\text{new}}$ is selected as the coherency matrix corresponding to volume scattering; the coefficients and their relationships are written as

$$\begin{aligned}
&f_\text{dv} = 2abs\left(T_{23}\right), f_\text{sv} = 2abs\left(T_{13}\right) \\
&f_\text{v} = \left[\frac{45-\cos 4\theta_\text{d}}{2rr\left(15+\cos 4\theta_\text{d}\right)} + \frac{1}{2}\right]\left(2T_{33} - f_\text{sv} - f_\text{dv}\right) \\
&S = f_\text{s} + f_\text{d}|\alpha|^2 = T_{11} - \frac{f_\text{v}}{2} - \frac{f_\text{sv}}{2} \\
&C = f_\text{s}\beta^* + f_\text{d}\alpha = T_{12} + \frac{f_\text{v}\cos 2\theta_\text{d}}{6} \\
&D = f_\text{s}|\beta|^2 + f_\text{d} = T_{22} - \frac{f_\text{dv}}{2} - \frac{\left(15-\cos 4\theta_\text{d}\right)f_\text{v}}{60}.
\end{aligned} \tag{29}$$

4) Volume Scattering Caused by Oriented Dihedral Scatterers: Similarly, when using the general volume scattering model caused by oriented dihedral scatterers, the coefficients and their relationships are derived as

$$\begin{aligned}
&f_\text{dv} = 2abs\left(T_{23}\right), f_\text{sv} = 2abs\left(T_{13}\right) \\
&f_\text{v} = \left[\frac{15-\cos 4\theta_\text{d}}{2rr\left(15+\cos 4\theta_\text{d}\right)} + \frac{1}{2}\right]\left(2T_{33} - f_\text{sv} - f_\text{dv}\right) \\
&S = f_\text{s} + f_\text{d}|\alpha|^2 = T_{11} - \frac{f_\text{sv}}{2} \\
&C = f_\text{s}\beta^* + f_\text{d}\alpha = T_{12} \\
&D = f_\text{s}|\beta|^2 + f_\text{d} = T_{22} - \frac{f_\text{dv}}{2} - \frac{\left(15-\cos 4\theta_d\right)f_\text{v}}{30}.
\end{aligned} \tag{30}$$

When $rr \le 1$, set $rr = 1$; (27)–(30) are suitable for the PolSAR data, and these equations are applicable to the P5SD.

III. Branch Conditions

A. Branch Condition for Volume Scattering Model Selection

According to the traditional decomposition methods, the selection of the volume scattering models depends on the value of $\text{Re}\{\langle S_\text{HH}S^*_\text{VV}\rangle\}$ [3]–[11]. In this article, different from these decomposition methods, the volume scattering model selection is determined by the building area extraction results. In the proposed method, θ_sv or θ_dv in the local area is similar and maintains a great consistent feature in the building areas, while forest and water areas show a completely random characteristics. Therefore, θ_sv or θ_dv can be used to extract the building candidates, and one of the angle parameters (θ_sv or θ_dv) is selected in different image. The images of θ_sv or θ_dv will be introduced in Section IV-B, and the consistency of the parameters can be illustrated intuitively. To quantitatively describe the local consistency of θ_sv or θ_dv, the n-order moment of difference value can be written as

$$LC^n_{(i,j)} = E\left\{D\left(\theta^k_\text{sv} - \theta^{(i,j)}_\text{sv})\right)^n\right\}, \quad k \in W(i,j) \tag{31}$$

where $\theta^{(i,j)}_\text{sv}$ is the θ_sv value in the ith row and the jth column of the image, and $W(i,j)$ is the selection window, which is similar to the refined Lee filter. θ^k_sv represents the local neighborhood elements of the $\theta^{(i,j)}_\text{sv}$ in window $W(i,j)$, and E denotes the mathematical expectation. If θ_dv is selected to extract the urban candidates, parameter θ_sv in (30) is replaced by θ_dv. To eliminate

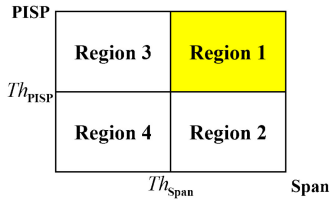

Fig. 4. PISP/Span division plane.

the phase wrapping, the distance D in (31) is

$$D(\theta) = \begin{cases} |\theta|, & |\theta| \le \pi \\ |\theta| - 2\pi, & \pi < |\theta| \le 2\pi. \end{cases} \tag{32}$$

The total power, namely, Span, is defined as the total backscattering power of the three mechanisms. Since the Span is invariant to change of basis, it can be used to classify scatters for various terrain types. According to [34], the PISP parameter is introduced to distinguish various terrain types with similar scattering characteristics. The Span can be used to distinguish the low-power and high-power regions, while the PISP is used to distinguish regions with different similarities. Therefore, the PISP and Span can be used as complement parameters to obtain the initial classification. In the PolSAR data, the building area candidates are identified using the appropriate thresholds of θ_{sv} or θ_{dv}, and Span. In the PolInSAR data, not only the appropriate threshold of θ_{sv} or θ_{dv} is used to identify the building area candidates, but the Span/PISP plane (shown in Fig. 4) can also be used to obtain the building candidates.

The PISP and Span are used as complement parameters to obtain the initial classification, and the image can be divided into four categories, as shown in Fig. 4. The Span is used to distinguish the low-power and high-power regions, while the PISP is used to distinguish regions with different similarities. In addition, the thresholds of Span and PISP can be defined as

$$\begin{aligned} \text{Th}_{\text{PISP}} &= \text{mean}\left(\text{PISP}\right) \\ \text{Th}_{\text{Span}} &= \text{mean}\left(\text{Span}\right). \end{aligned} \tag{33}$$

After the thresholds of Span and PISP are determined, the image is divided into four regions, and the scattering characteristics are listed as follows.

Region 1: In this region, both PISP and Span have large values. The typical scattering mechanisms are double-bounce scattering and surface scattering, which are produced by the buildings with various orientation angles and the ground-trunk dihedral structures in the forest.

Region 2: In this region, the value of PISP is small and the value of Span is large. The dominant scattering mechanism is volume scattering, which is produced by vegetation areas composed of branches and leaves.

Region 3: In this region, the value of PISP is large and the value of Span is small. The dominant scattering mechanism is surface scattering, and the value of signal-to noise ratio is large. This region can be used to characterize crops and some types of rocks.

Region 4: In this region, the values of PISP and Span are small. This region can be used to characterize roads and airport runway.

According to the classification results of the scattering characteristics, the samples in region 1 can be recognized as the building area candidates, and the classification results can be used as the branch condition for selecting the reasonable volume scattering model of various land covers.

B. Branch Condition for Double-Bounce/Surface Scattering

Similar to the traditional four-component decomposition method, the dominant scattering mechanism (the double-bounce scattering or the surface scattering) of the matrix depends on the value of $\text{Re}\{\langle S_{\text{HH}} S_{\text{VV}}^{*} \rangle\}$ [3]. The criteria, namely, C_1, can be derived as

$$C_1 = T_{11} - T_{22} - T_{33} + P_{\text{dv}} = 2T_{11} + P_{\text{dv}} - \text{Span}. \tag{34}$$

If $C_1 > 0$, surface scattering is the dominant mechanism. Since the double-bounce component is negligible, the value of α can be assumed to be $\alpha = 0$. In this condition, the solutions of the undetermined equations are

$$f_{\text{s}} = S, \beta^{*} = C/S, f_{\text{d}} = D - |C|^2/S. \tag{35}$$

If $C_1 \le 0$, double-bounce scattering is the dominant mechanism. Since the surface component is negligible, the value of $|\beta|$ can be assumed to be $\beta = 0$. In this condition, the solutions of the undetermined equations are

$$f_{\text{d}} = D, \alpha = C/D, f_{\text{s}} = S - |C|^2/D. \tag{36}$$

Once the coefficients are determined, the scattering powers can be expressed as

$$\begin{aligned} &P_{\text{s}} = f_{\text{s}}\left(1 + |\beta|^2\right), P_{\text{d}} = f_{\text{d}}\left(1 + |\alpha|^2\right) \\ &P_{\text{v}} = f_{\text{v}}, P_{\text{sv}} = f_{\text{sv}}, P_{\text{dv}} = f_{\text{dv}}. \end{aligned} \tag{37}$$

In addition, the scattering powers are equally applicable to the oriented dihedral scattering areas. The entire flowchart of the PI5SD is shown in Fig. 5. When $rr \le 1$, the image shown in Fig. 5 is the flowchart of the P5SD.

To reasonably visualize the scattering mechanisms of various land covers, the power redistribution rule of the P5SD and PI5SD can be described as follows.

1) For the extracted building areas, the power redistribution rule is

$$P_{\text{s}}^{\text{total}} = P_{\text{s}} + \frac{P_{\text{sv}}}{2}, P_{\text{v}}^{\text{total}} = P_{\text{v}}, P_{\text{s}}^{\text{total}} = P_{\text{d}} + P_{\text{dv}} + \frac{P_{\text{sv}}}{2}. \tag{38}$$

2) For other regions, the power redistribution rule is

$$\begin{aligned} P_{\text{v}}^{\text{total}} &= P_{\text{v}} + \frac{P_{\text{dv}}}{2} + \frac{P_{\text{sv}}}{2} \\ P_{\text{s}}^{\text{total}} &= P_{\text{s}} + \frac{P_{\text{sv}}}{2}, P_{\text{s}}^{\text{total}} = P_{\text{d}} + \frac{P_{\text{dv}}}{2}. \end{aligned} \tag{39}$$

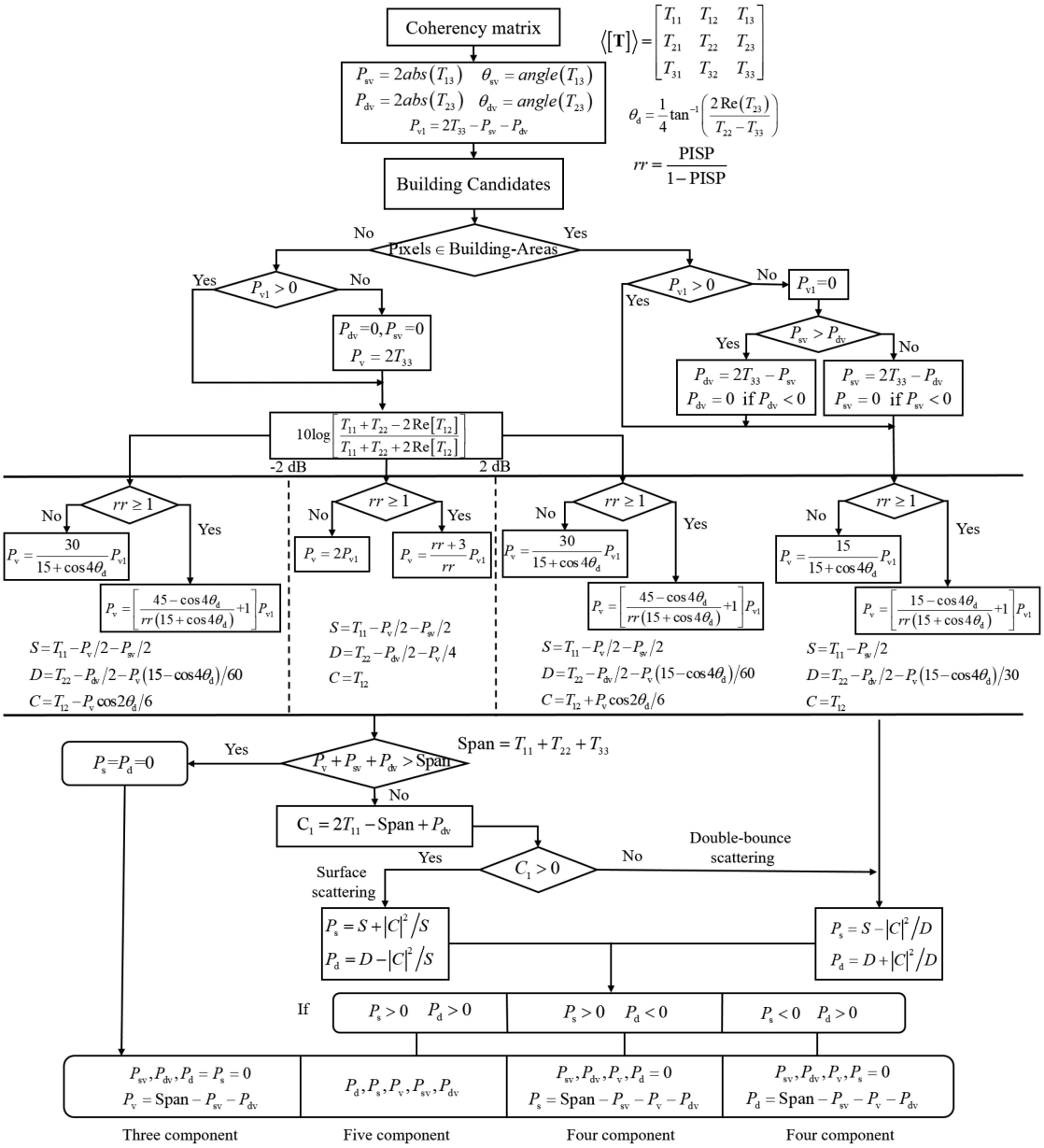

Fig. 5. Flowchart of the model-based five-component decomposition method of PolInSAR (PI5SD). When $rr \leq 1$, this image is the flowchart of the P5SD.

IV. Results and Discussions

A. Study Site

In this article, L-band E-SAR repeat-pass PolInSAR datasets are used to evaluate the performance of the P5SD and PI5SD. The study site is over the Oberpfaffenhofen, Germany, which includes buildings with various orientation angles, roads, forests, and airports. This image has a dimension of 1300×1200 pixels, and the temporal baseline is within one day. The incidence angle is about 40°, and the geolocation center is ($48^\circ5'3''$N, $11^\circ17'4''$E). As the equivalent number of looks of the data is high enough, no more averaging or filter is employed. The optical image of the study site and the corresponding Pauli RGB pseudo color image are shown in Fig. 6(a) and (b), respectively.

B. Building Area Extraction

In the proposed method, the value of n in (31) is set to 2, and the images of θ_{sv} and θ_{dv} are shown in Fig. 7(a) and (b), respectively. The legend of the images represents the angle value in range $[-\pi, \pi]$. According to these images, since θ_{dv} shows different characteristics in urban and nonurban areas, it is selected to reasonable extract the building candidates.

Moreover, the PISP/Span plane is used as the criteria for selecting the volume scattering models in the PolInSAR image. The maps of Span and PISP are shown in Fig. 8(a) and (b), respectively. In Fig. 8(a), the scattering power of the double-bounce scattering and volume scattering is strong. The dominant scattering mechanism of the ground-wall structure in urban area and the trunk-ground scattering in forests is double-bounce

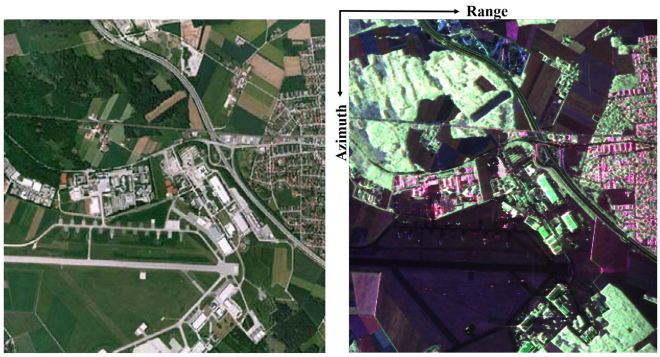

Fig. 6. SAR images of the study site over the Oberpfaffenhofen, Germany (E-SAR, L-band). (a) Optical image from Google Earth. (b) Corresponding color-coded Pauli decomposition with red (double-bounce), green (volume scattering), and blue (surface scattering).

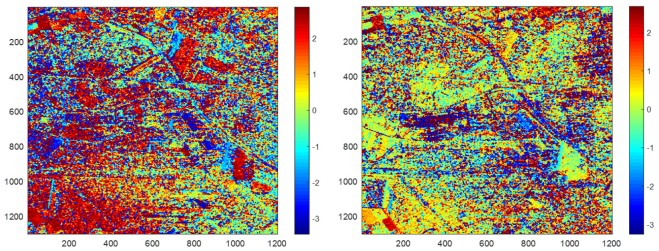

Fig. 7. Angle maps of the coupling forms. (a) Coupling form θ_{sv} of the coherency element T_{13}. (b) Coupling form θ_{dv} of the coherency element T_{23}.

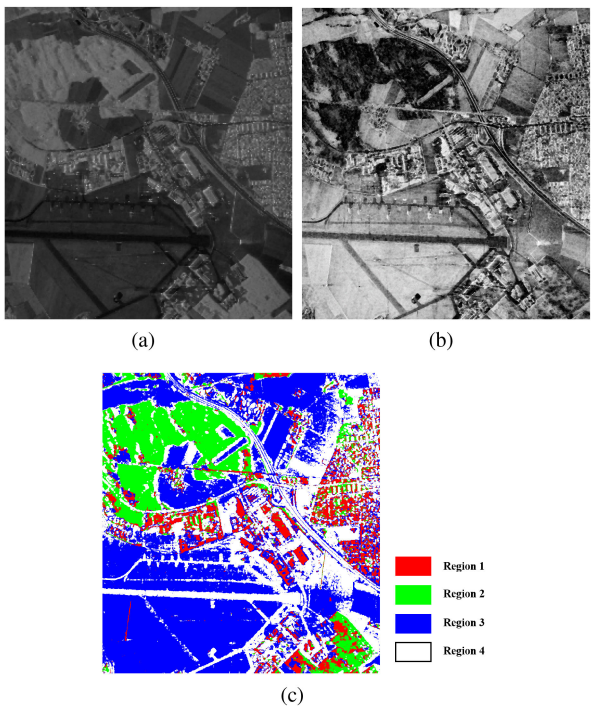

Fig. 8. E-SAR PolInSAR magnitudes. (a) Span image. (b) PISP image. (c) Initial classification results using the PISP/Span plane.

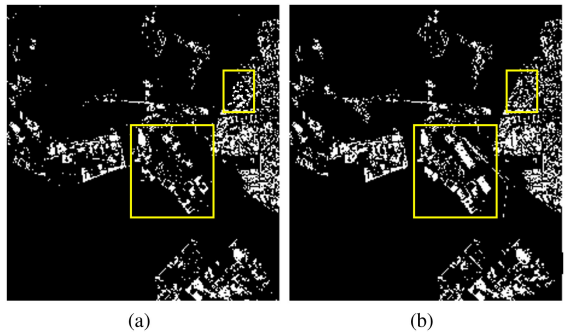

Fig. 9. Extraction results of PolSAR and PolInSAR data (white: building pixels, black: others). (a) Building areas extraction map of PolSAR. (b) Building areas extraction map of PolInSAR.

scattering. The strength of the surface scattering depends on the value of incident angle and the roughness of the surface. For the areas with low roughness, the surface scattering cross-pol component is usually not considered. When the incident angle is close to 0°, the scattering power of surface scattering is very strong (such as buildings perpendicular to the incident direction). When the incident angle is close to 90°, the scattering power of surface scattering is weak (such as flat roads and crops). Some of the terrain types can be identified using an appropriate threshold of Span. However, the Span cannot effectively distinguish some land coves with similar scattering characteristics, such as buildings with large orientation angles and forests. In Fig. 8(b), the value of building area is large and the value of forest is small. This performance can be explained as: the dominant scattering mechanisms of building areas are double-bounce scattering and wire scattering, the scattering characteristics remain unchanged during the interferometric imaging, while the dominant mechanism in forest areas is random scattering. Therefore, the PISP/Span plane can be used to obtain the initial segmentation, and the image can be divided into four categories; the initial classification map is shown in Fig. 8(c).

In Fig. 8(c), the forests and buildings with large orientation angles are appropriately divided into two categories, indicating that the classification map is a reasonable approach. In Region 1, since the sample points characterize the buildings with various orientation angles, the volume scattering model caused by the oriented dihedral scatter is selected. In other regions, the volume scattering model selection is determined by the ratio of $|S_{\mathrm{HH}}|^2$ to $|S_{\mathrm{VV}}|^2$. Therefore, this classification results can be used to select the volume scattering models. To evaluate the performance of this branch condition, the extraction maps of PolSAR using θ_{dv} and Span, and PolInSAR image using θ_{dv} and PISP/Span plane are shown in Fig. 9(a) and (b), respectively. In Fig. 9, compared with the extraction map of PolSAR data, more building areas with large orientation angles can be extracted as candidate areas in the extraction map of PolInSAR data (marked in yellow rectangles shown in Fig. 9), and the vegetated areas do not interfere with the extraction results.

C. Decomposition Results

The entire polarimetric decomposition image obtained via P5SD is shown in Fig. 10(a). To demonstrate the effectiveness

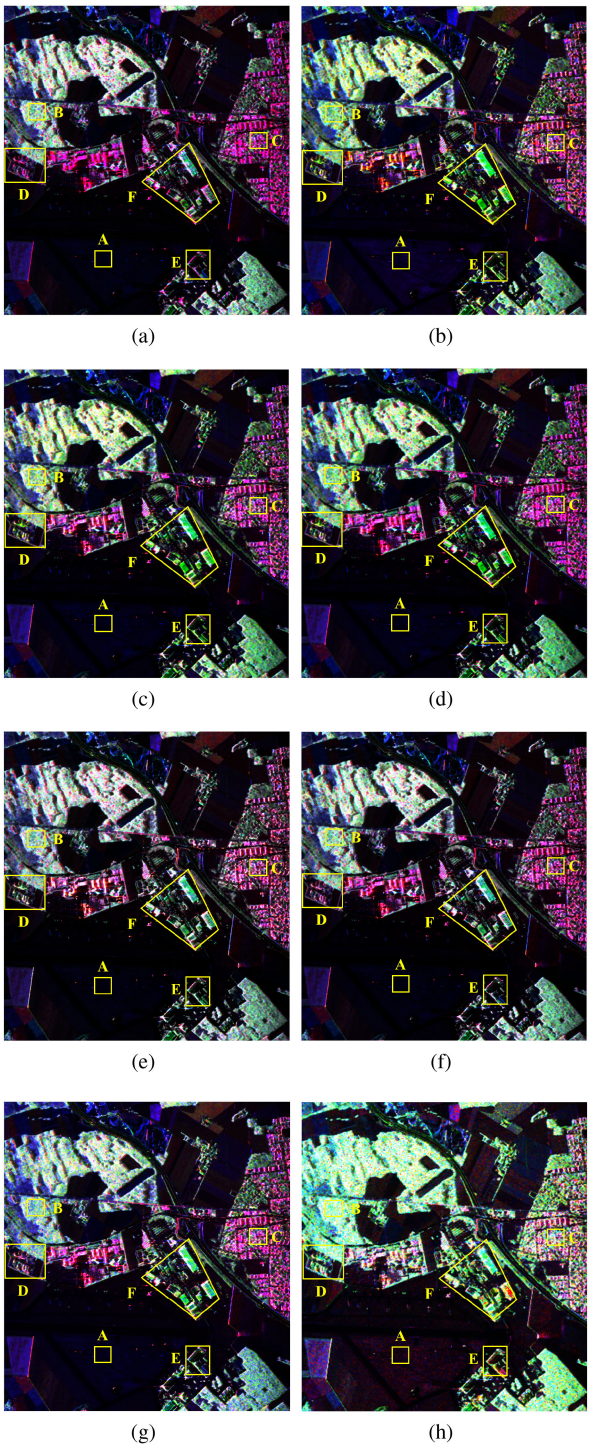

Fig. 10. Decomposition results using (a) P5SD, (b) FDD, (c) Y4R, (d) G4U, (e) 6SD, (f) 7SD, (g) ExG4URcc, and (h) MCSMs. Red (double-bounce scattering), green (volume scattering), and blue (surface scattering).

of the refined volume scattering models, the decomposition map obtained via the P5SD is compared with the FDD, Y4R, G4U, 6SD, 7SD, ExG4URcc, and MCSMs. The decomposition results using these eight decomposition methods are shown in Fig. 10. The dominant mechanism of vegetation areas is volume scattering and the dominant mechanism of farmland is surface area.

Fig. 11. Enlarged optical images of the selected patches. (a) Patch A. (b) Patch B. (c) Patch C. (d) Patch D. (e) Patch E. (f) Patch F.

TABLE I
SCATTERING POWER CONTRIBUTION (%) FOR PATCH A

	P_{d}	P_{s}	P_{v}	P_{c}	P_{w}	P_{cd}	P_{od}	P_{md}	P_{sv}	P_{dv}
FDD	4.8	81.7	13.5	–	–	–	–	–	–	–
Y4R	4.9	81.6	12.3	1.2	–	–	–	–	–	–
G4U	5.1	82.4	11.3	1.2	–	–	–	–	–	–
6SD	2.3	84.7	10.7	0.8	–	0.7	0.8	–	–	–
7SD	2.1	84.5	11.0	0.6	–	0.7	0.5	0.6	–	–
ExG4URcc	4.7	83.0	11.1	1.2	–	–	–	–	–	–
MCSMs	3.9	82.5	11.3	0.7	1.6	–	–	–	–	–
P5SD	4.2	83.5	9.6	–	–	–	–	–	1.7	1.0

TABLE II
SCATTERING POWER CONTRIBUTION (%) FOR PATCH B

	P_{d}	P_{s}	P_{v}	P_{c}	P_{w}	P_{cd}	P_{od}	P_{md}	P_{sv}	P_{dv}
FDD	2.9	20.3	76.8	–	–	–	–	–	–	
Y4R	3.4	19.4	71.9	5.3	–	–	–	–	–	
G4U	6.5	20.4	67.8	5.3	–	–	–	–	–	
6SD	7.5	22.9	52.0	4.9	6.1	6.6	–	–	–	
7SD	6.9	23.8	49.7	4.9	5.4	5.3	4.0	–	–	
ExG4URcc	6.5	19.9	68.4	5.2	–	–	–	–	–	–
MCSMs	2.4	18.5	71.1	4.8	3.2	–	–	–	–	–
P5SD	8.0	26.7	45.1	–	–	–	–	11.8	8.4	

In Fig. 10, compared with the existing decomposition methods, the contribution of volume scattering is significantly reduced in the P5SD and the building areas with various orientation angles become "redder." The scattering mechanisms of the image with various land covers can be reasonably interpreted.

To quantitatively evaluate the performance of the P5SD, six patches are selected, as shown in Fig. 10. The terrain types of A, B, and C are farmland, forest, and orthogonal buildings, respectively. The terrain types of patches D, E, and F are the oriented buildings with various orientation angles. The enlarged optical images of these patches are shown in Fig. 11. The mean power statistics of these patches are listed in Tables I–VI, respectively.

For the farmland and runway, the dominant scattering mechanism is surface scattering, and the percentage contribution of surface scattering is 81.7%, 81.6%, 82.4%, 84.7%, 84.5%, 83.0%, 82.5%, and 83.5% for FDD, Y4R, G4U, 6SD, 7SD, ExG4URcc, MCSMs, and P5SD, respectively. For the vegetated areas, the dominant scattering mechanism is volume scattering, and the percentage contribution of volume scattering is 76.8%,

TABLE III
SCATTERING POWER CONTRIBUTION (%) FOR PATCH C

	P_{d}	P_{s}	P_{v}	P_{c}	P_{w}	P_{cd}	P_{od}	P_{md}	P_{sv}	P_{dv}
FDD	63.1	30.7	6.2	–	–	–	–	–	–	
Y4R	64.4	31.8	3.2	0.6	–	–	–	–	–	
G4U	64.7	32.0	2.7	0.6	–	–	–	–	–	
6SD	64.2	31.8	2.2	0.6	0.4	0.8	–	–	–	
7SD	62.5	31.4	1.2	1.1	1.3	1.2	1.3	–	–	
ExG4URcc	64.6	32.4	2.4	0.6	–	–	–	–	–	–
MCSMs	64.4	32.0	2.9	0.4	0.3	–	–	–	–	–
P5SD	64.6	31.5	0.9	–	–	–	–	1.1	1.9	

TABLE IV
SCATTERING POWER CONTRIBUTION (%) FOR PATCH D

	P_{d}	P_{s}	P_{v}	P_{c}	P_{w}	P_{cd}	P_{od}	P_{md}	P_{sv}	P_{dv}
FDD	16.1	26.7	57.2	–	–	–	–	–	–	–
Y4R	17.1	27.4	49.6	5.9	–	–	–	–	–	–
G4U	26.9	29.4	37.8	5.9	–	–	–	–	–	–
6SD	29.2	34.4	24.7	5.0	–	3.1	3.6	–	–	–
7SD	30.0	33.5	22.6	4.1	–	3.1	3.3	3.4	–	–
ExG4URcc	28.3	33.4	32.4	5.9	–	–	–	–	–	–
MCSMs	21.8	28.7	41.5	4.1	3.9	–	–	–	–	–
P5SD	29.9	33.3	14.5	–	–	–	–	–	12.6	9.7

TABLE V
SCATTERING POWER CONTRIBUTION (%) FOR PATCH E

	P_{d}	P_{s}	P_{v}	P_{c}	P_{w}	P_{cd}	P_{od}	P_{md}	P_{sv}	P_{dv}
FDD	11.5	27.6	60.9	–	–	–	–	–	–	–
Y4R	17.7	31.3	44.7	6.3	–	–	–	–	–	–
G4U	31.7	38.4	23.6	6.3	–	–	–	–	–	–
6SD	34.3	33.0	15.7	6.5	–	5.1	5.4	–	–	–
7SD	33.9	31.6	11.1	6.6	–	5.4	5.6	5.8	–	–
ExG4URcc	31.5	36.0	26.2	6.3	–	–	–	–	–	–
MCSMs	26.9	33.2	29.8	4.4	5.7	–	–	–	–	–
P5SD	34.1	32.4	10.9	–	–	–	–	–	12.5	10.1

TABLE VI
SCATTERING POWER CONTRIBUTION (%) FOR PATCH F

	P_{d}	P_{s}	P_{v}	P_{c}	P_{w}	P_{cd}	P_{od}	P_{md}	P_{sv}	P_{dv}
FDD	11.4	24.5	64.1	–	–	–	–	–	–	–
Y4R	12.0	39.3	42.2	6.5	–	–	–	–	–	–
G4U	14.8	42.1	36.6	6.5	–	–	–	–	–	–
6SD	16.1	42.3	23.7	7.0	–	6.1	4.8	–	–	–
7SD	15.2	38.4	21.8	6.6	–	6.2	6.8	5.0	–	–
ExG4URcc	15.9	42.5	35.1	6.5	–	–	–	–	–	–
MCSMs	13.2	36.4	36.7	3.3	10.4	–	–	–	–	–
P5SD	16.1	27.5	19.4	–	–	–	–	–	28.7	8.3

TABLE VII
SCATTERING POWER CONTRIBUTION (%) FOR ROI-I

	P_{d}	P_{s}	P_{v}	P_{c}	P_{w}	P_{cd}	P_{od}	P_{md}	P_{sv}	P_{dv}
FDD	40.2	28.9	30.9	–	–	–	–	–	–	–
Y4R	41.4	29.7	26.4	2.5	–	–	–	–	–	–
G4U	42.1	31.1	24.3	2.5	–	–	–	–	–	–
6SD	41.3	31.6	22.4	2.1	–	1.3	1.3	–	–	–
7SD	41.2	31.2	22.1	2.0	–	1.2	1.2	1.1	–	–
ExG4URcc	42.2	32.2	23.1	2.5	–	–	–	–	–	–
MCSMs	41.9	30.3	24.0	1.1	2.7	–	–	–	–	–
P5SD	42.8	31.5	20.5	–	–	–	–	–	3.1	2.1
PI5SD	43.7	31.2	19.6	–	–	–	–	–	3.3	2.2

71.9%, 67.8%, 52.0%, 49.7%, 68.4%, 71.1%, and 45.1% for FDD, Y4R, G4U, 6SD, 7SD, ExG4URcc, MCSMs, and P5SD, respectively. In the 6SD and 7SD, volume scattering is also included in the compound scattering components (P_{od} and P_{cd}) generated by term T_{13} and the compound scattering components (P_{c} and P_{hr}) generated by term T_{23}. Similarly, the volume scattering is included in the coupling scattering components (P_{sv} and P_{dv}) in the P5SD. All the previously described eight decomposition methods can be used to interpret the dominant scattering mechanisms of vegetated areas and farmland.

Buildings in patch C are orthogonal or approximately orthogonal to the LOS and the dominant scattering is double-bounce scattering. The statistics demonstrate 63.1%, 64.4%, 64.7%, 64.2%, 62.5%, 64.6%, 64.4%, and 64.6% of double-bounce scattering in FDD, Y4R, G4U, 6SD, 7SD, ExG4URcc, MCSMs, and P5SD, respectively. In addition, the double-bounce scattering is also included in the compound scattering components (P_{c} and P_{hr}) generated by term T_{23} in 6SD and 7SD and the coupling scattering components (P_{dv}) in P5SD. In Table III, the contributions of P_{c}, P_{sv}, and P_{dv} are small, which means that the cross-pol component is not the dominant scattering mechanism.

Patches D, E, and F are the oriented building areas with different orientation angles, as shown in Fig. 11(d)–(f). The rotation of these building areas leads to the increase of the cross-pol component. Using the P5SD, these three patches are all looks "redder" than the images obtained via the existing decomposition methods.

For patch D, P_{d} contributes 16.1%, 17.1%, 26.9%, 29.2%, 30.0%, 28.3%, 21.8%, and 29.9% for FDD, Y4R, G4U, 6SD, 7SD, ExG4URcc, MCSMs, and P5SD, respectively. In Table IV, the P_{d} contributions of existing decomposition methods are higher than those of the P5SD. This phenomenon can be explained as follows: the reflection symmetry assumption is not satisfied in the oriented building areas and the double-bounce scattering component is also contained in the coupling terms (P_{dv}) to characterize the dominant scattering mechanism of the oriented buildings.

For patch E, the orientation angle is larger than that in patch D, and the statistics demonstrate 11.5%, 17.7%, 31.7%, 34.3%, 33.9%, 31.5%, 26.9%, and 34.1% of double-bounce scattering in FDD, Y4R, G4U, 6SD, 7SD, ExG4URcc, MCSMs, and P5SD, respectively. According to Table V, the reduced volume scattering is transformed into the surface scattering and double-bounce scattering, which can be used to characterize the dominant scattering mechanism of building areas. In Fig. 9(a), buildings in patch E are colored in red, which are consistent with the ground truth.

The orientation angle of the buildings in patch F is about 45° and the OAC operation is no longer valid in this area. The double-bounce scattering cannot be recognized by the methods with the OAC. The percentage contribution of double-bounce scattering is 11.4%, 12.0%, 14.8%, 16.1%, 15.2%, 15.9%, 13.2%, and 16.1% for FDD, Y4R, G4U, 6SD, 7SD, ExG4URcc, MCSMs, and P5SD, respectively. Compared with the existing polarimetric decomposition methods, the volume scattering component of P5SD is reduced by 44.7%, 22.8%, 17.2%, 4.3%, 2.4%, 15.7%, and 17.3%, respectively. The P_{sv} component contributes 28.7%

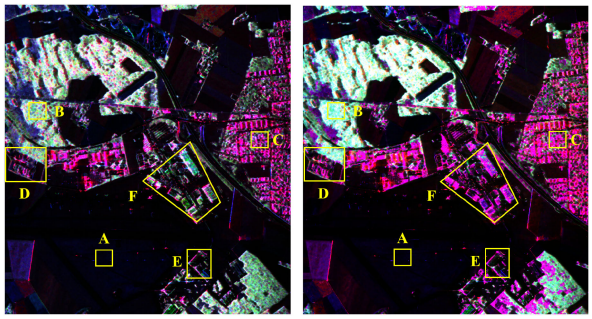

Fig. 12. Decomposition results using (a) P5SD and (b) PI5SD.

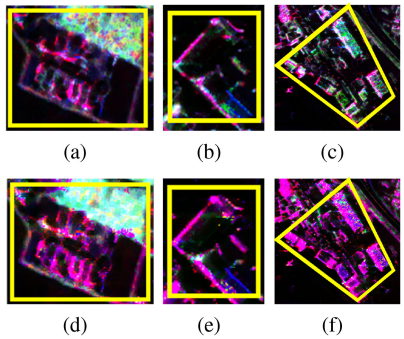

Fig. 13. Enlarged decomposition results of patches D, E, and F. (a)–(c) Decomposition results of patches D, E, and F obtained via P5SD. (d)–(f) Decomposition results of patches D, E, and F obtained via PI5SD.

and the P_{dv} component contributes 8.3%, which means that the coupling scattering components play important roles in the building areas with large orientation angles. The coupling terms can be characterized as the indicators of the scattering mechanism. Therefore, the P5SD can be used to characterize the scattering mechanism of the building areas with large orientation angles, and the decomposition results shown in Fig. 9(a) demonstrate that the dominant scattering of this area can be reasonably interpreted.

Compared with 6SD and 7SD, the decomposition results obtained via P5SD have better performance in case of oriented buildings; this phenomenon can be explained as follows: 1) Compared with the 6SD, the P5SD utilizes the information of the whole image data and all the elements of the coherency matrix, which can get better decomposition results. In addition, before the decomposition, the 6SD employs the OAC, which may lead to the occurrence of errors. 2) In the P5SD, feature θ_{sv} or θ_{dv} is embedded in the building area identification, and the building extraction results are used as the branch condition of the volume scattering model selection. In 6SD and 7SD, the branch conditions are similar to that in the traditional decomposition method. If the threshold selection results of P5SD are more reasonable than that of 6SD and 7SD, better decomposition results can be obtained via P5SD. Therefore, P5SD has advantages in characterizing the scattering mechanisms of various terrain types.

In this article, according to the previously described analyses, the PISP is introduced to further modify the refined volume scattering models so that the five-component decomposition method can be applied to the PolInSAR data. The performance of the five-component decomposition method of PolInSAR (PI5SD) is evaluated by comparing with the P5SD, and the entire decomposition image of PI5SD is shown in Fig. 12(b). The enlarged decomposition results (obtained via P5SD and PI5SD) of the oriented building areas (patches D, E, and F) are shown in Fig. 13, and the mean power statistics of these patches are shown in Fig. 14.

According to Fig. 14, the volume scattering component obtained via PI5SD can be further reduced, and the contribution of double-bounce scattering increases. In addition, the coupling scattering components (P_{sv} and P_{dv}) obtained via PI5SD increase, and these components can be used to enhance the performance of the decomposition method. Therefore, for the oriented building areas, especially the building areas with large orientation angles, the PI5SD can be used to characterize the scattering mechanisms of various land covers more reasonably by employing the interferometric information, and the OVS can be overcome.

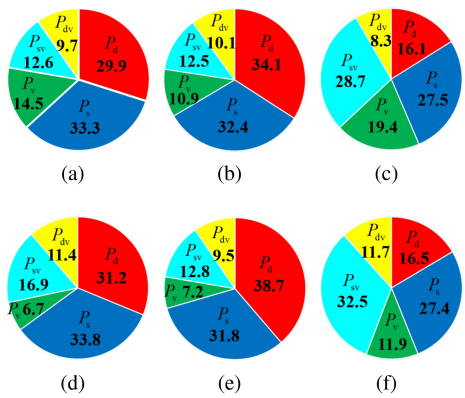

Fig. 14. Mean power statistics of the oriented building patches D, E, and F. (a) and (d) Mean power statistics of patch D using P5SD and PI5SD. (b) and (e) Mean power statistics of patch E using P5SD and PI5SD. (c) and (f) Mean power statistics of patch F using P5SD and PI5SD.

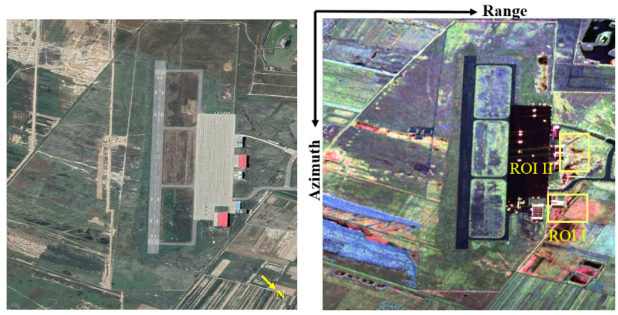

Fig. 15. SAR images of the study site over Xi'an, China (Airborne, C-band). (a) Optical image from Google Earth. (b) Corresponding color-coded Pauli decomposition with red (double-bounce), green (volume scattering), and blue (surface scattering).

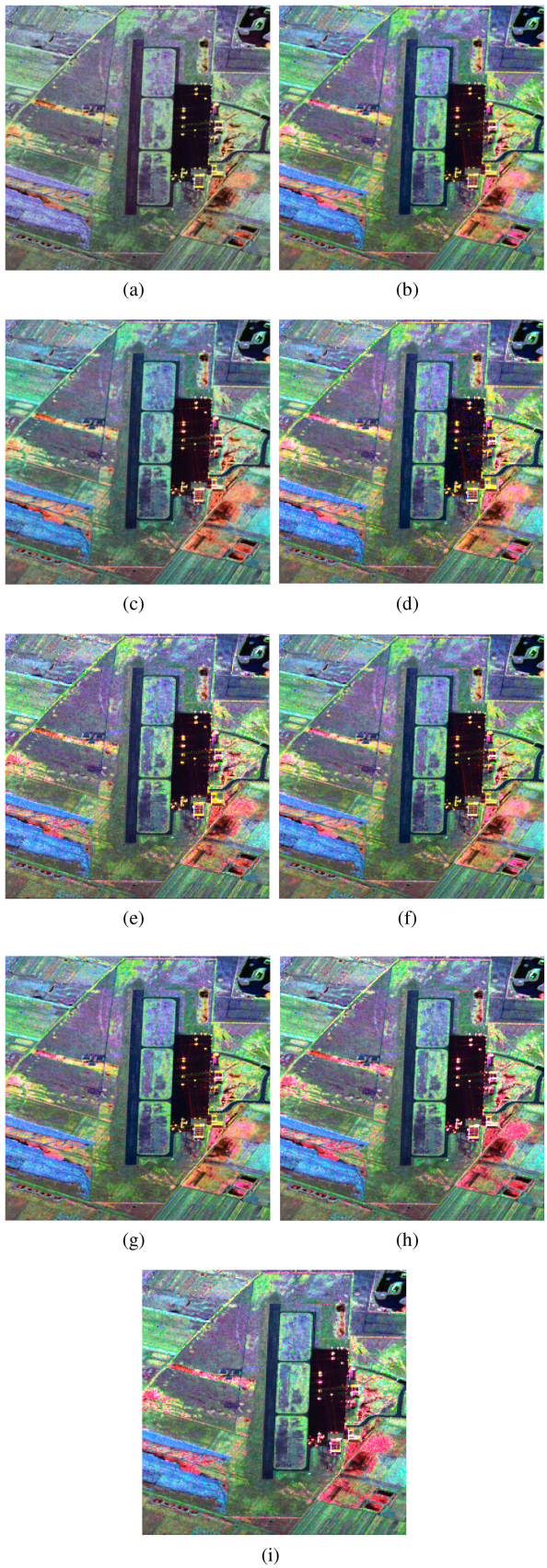

Fig. 16. Decomposition results using (a) FDD, (b) Y4R, (c) G4U, (d) 6SD, (e) 7SD, (f) ExG4URcc, (g) MCSMs, (h) P5SD, and (i) PI5SD.

TABLE VIII
SCATTERING POWER CONTRIBUTION (%) FOR ROI-II

	P_{d}	P_{s}	P_{v}	P_{c}	P_{w}	P_{cd}	P_{od}	P_{md}	P_{sv}	P_{dv}
FDD	11.7	30.9	57.4	–	–	–	–	–	–	–
Y4R	12.5	31.2	53.1	3.2	–	–	–	–	–	–
G4U	13.9	31.5	51.4	3.2	–	–	–	–	–	–
6SD	14.0	32.2	47.7	2.7	–	1.6	1.8	–	–	–
7SD	14.2	32.4	47.1	2.4	–	1.3	1.2	1.4	–	–
ExG4URcc	14.0	33.5	49.3	3.2	–	–	–	–	–	–
MCSMs	13.2	30.3	51.9	1.4	3.2	–	–	–	–	–
P5SD	15.6	32.1	43.4	–	–	–	–	–	4.8	4.1
PI5SD	16.2	32.3	42.6	–	–	–	–	–	4.7	4.2

D. PolInSAR Data Obtained by the Chinese Academy of Sciences

To further demonstrate the validity of the P5SD and PI5SD, experiments are conducted on the airborne C-band PolInSAR data that were collected by the AIR, over Xi'an, China. The master and slave datasets are collected simultaneously, and these datasets are highly correlated. The image size is 2479×2473 pixels, and the spatial resolution of these data is 2.43 m×2.08 m. The incidence angle is about 40°. The optical image and the Pauli RGB image are shown in Fig. 15. The decomposition results obtained via aforementioned nine decomposition methods (FDD, Y4R, G4U, 6SD, 7SD, ExG4URcc, MCSMs, P5SD, and PI5SD) are shown in Fig. 16.

For statistical analysis, two patches shown in Fig. 15(b) are selected as the regions of interest (ROIs), and the contributions of the scattering powers are listed in Tables VII and VIII, respectively. In Tables VII and VIII, the volume scattering power can be properly reduced, and the double-bounce scattering and surface scattering are correspondingly increases, accordingly, using P5SD and PI5SD. The decomposition results obtained via the P5SD and PI5SD can better interpret the scattering mechanisms of the land covers, and the OVS can be properly overcome. Compared with the polarimetric decomposition method, the OVS can be further overcome by using the PI5SD, which means that the interferometric information is important to describe the scattering mechanism of the building areas with large orientation angles.

V. CONCLUSION

In this article, five-component decomposition methods of PolSAR and PolInSAR using coupling scattering models are proposed to characterize the scattering mechanisms of various terrain types. Refined volume scattering models are introduced to reduce the volume scattering of the building areas with large orientation angles and are further modified using the PISP in the PolInSAR image. The coupling scattering models are proposed to physically interpret the T_{13} and T_{23} terms of the coherency matrix. Angle $\theta_{\mathrm{sv}}/\theta_{\mathrm{dv}}$ and Span in the PolSAR image (angle $\theta_{\mathrm{sv}}/\theta_{\mathrm{dv}}$ and Span/PISP plane in the PolInSAR image) are used to extract the urban candidates so that the suitable volume scattering model can be selected. According to the decomposition results obtained via the P5SD and PI5SD, P_{sv} and P_{dv} are

significant in interpreting the scattering mechanisms in building areas with large orientation angles, and all elements of the coherency matrix are considered. Compared with the P5SD, the PI5SD has advantages in overcoming the OVS by considering interferometric information. The experimental results demonstrate that the P5SD has advantages over existing polarimetric decomposition methods, and the PI5SD yields satisfactory decomposition results for building areas, especially the building areas with large orientation angles. Therefore, the P5SD and PI5SD, which overcome the OVS and mitigate the ambiguity of the scattering mechanism in urban areas, are effective decomposition approaches of the PolSAR and PolInSAR data, respectively.

REFERENCES

[1] S. R. Cloude and E. Pottier, "An entropy based classification scheme for land applications of polarinetric SAR," *IEEE Trans. Geosci. Remote Sens.*, vol. 35, no. 1, pp. 68–78, Jan. 1997.

[2] R. Touzi, "Target scattering decomposition in terms of roll-invariant target parameters," *IEEE Trans. Geosci. Remote Sens.*, vol. 45, no. 1, pp. 73–84, Jan. 2007.

[3] A. Freeman and S. L. Durden, "A three-component scattering model for polarimetric SAR data," *IEEE Trans. Geosci. Remote Sens.*, vol. 36, no. 3, pp. 963–973, May 1998.

[4] Y. Yamaguchi, T. Moriyama, M. Ishido, and H. Yamada, "Four-component scattering model for polarimetric SAR image decomposition," *IEEE Trans. Geosci. Remote Sens.*, vol. 43, no. 8, pp. 1699–1706, Aug. 2005.

[5] L. Zhang, B. Zou, H. Cai, and Y. Zhang, "Multiple-component scattering model for polarimetric SAR image decomposition," *IEEE Geosci. Remote Sens. Lett.*, vol. 5, no. 4, pp. 603–607, Oct. 2008.

[6] Y. Yamaguchi, A. Sato, W. M. Boerner, R. Sato, and H. Yamada, "Four-component scattering power decomposition with rotation of coherency matrix," *IEEE Trans. Geosci. Remote Sens.*, vol. 49, no. 6, pp. 2251–2258, Jun. 2011.

[7] J. J. van Zyl, M. Arii, and Y. Kim, "Model-based decomposition of polarimetric SAR covariance matrices constrained for nonnegative eigenvalues," *IEEE Trans. Geosci. Remote Sens.*, vol. 49, no. 9, pp. 3452–3459, Sep. 2011.

[8] A. Sato, Y. Yamaguchi, G. Singh, and S. Park, "Four-component scattering power decomposition with rotation of coherency matrix," *IEEE Geosci. Remote Sens. Lett.*, vol. 9, no. 2, pp. 166–170, Mar. 2012.

[9] G. Singh, Y. Yamaguchi, and S. E. Park, "General four-component scattering power decomposition with unitary transformation of coherency matrix," *IEEE Trans. Geosci. Remote Sens.*, vol. 51, no. 5, pp. 3014–3022, Feb. 2013.

[10] G. Singh and Y. Yamaguchi, "Model-based six-component scattering matrix power decomposition," *IEEE Trans. Geosci. Remote Sens.*, vol. 56, no. 10, pp. 5687–5704, Oct. 2018.

[11] G. Singh *et al.*, "Seven-component scattering power decomposition of POLSAR coherency matrix," *IEEE Trans. Geosci. Remote Sens.*, vol. 57, no. 11, pp. 8371–8382, Nov. 2019.

[12] J. J. Sharma, I. Hajnsek, K. P. Papathanassiou, and A. Moreira, "Polarimetric decomposition over glacier ice using long-wavelength airborne PolSAR," *IEEE Trans. Geosci. Remote Sens.*, vol. 49, no. 1, pp. 519–535, Jan. 2011.

[13] J. Kim, D. Kim, and B. J. Hwang, "Characterization of arctic sea ice thickness using high-resolution spaceborne polarimetric SAR data," *IEEE Trans. Geosci. Remote Sens.*, vol. 50, no. 1, pp. 13–22, Jan. 2012.

[14] X. Zhang, W. Dierking, J. Zhang, and J. Meng, "A polarimetric decomposition method for ice in the Bohai Sea using C-band PolSAR data," *IEEE Trans. Geosci. Remote Sens.*, vol. 8, no. 1, pp. 47–66, Jan. 2015.

[15] I. Hajnsek, T. Jagdhuber, H. Schon, and K. P. Papathanassiou, "Potential of estimating soil moisture under vegetation cover by means of PolSAR," *IEEE Trans. Geosci. Remote Sens.*, vol. 47, no. 2, pp. 442–454, Feb. 2009.

[16] T. Jagdhuber, I. Hajnsek, and K. P. Papathanassiou, "An iterative generalized hybrid decomposition for soil moisture retrieval under vegetation cover using fully polarimetric SAR," *IEEE J. Sel. Topics Appl. Earth Observ. Remote Sens.*, vol. 8, no. 8, pp. 3911–3922, Aug. 2015.

[17] G. D. Martino, A. lodice, A. Natale, and D. Riccio, "Polarimetric two-scale two-component model for the retrieval of soil moisture under moderate vegetation via L-band SAR data," *IEEE Trans. Geosci. Remote Sens.*, vol. 54, no. 4, pp. 2470–2491, Apr. 2016.

[18] H. Wang, R. Magagi, K. Goita, and T. Jagdhuber, "Refining a polarimetric decomposition of multi-angular UAVSAR time series for soil moisture retrieval over low and high vegetated agricultural fields," *IEEE Trans. Geosci. Remote Sens.*, vol. 12, no. 5, pp. 1431–1450, May 2019.

[19] S. Chen and M. Sato, "Tsunami damage investigation of built-up areas using multitemporal spaceborne full polarimetric SAR images," *IEEE Trans. Geosci. Remote Sens.*, vol. 51, no. 4, pp. 1985–1997, Apr. 2013.

[20] Y. Ji, J. T. S. Sumantyo, M. Y. Chua, and M. M. Waqar, "Earthquake/tsunami damage level mapping of urban areas using full polarimetric SAR data," *IEEE J. Sel. Topics Appl. Earth Observ. Remote Sens.*, vol. 11, no. 7, pp. 2296–2309, Jul. 2018.

[21] D. Xiang, W. Wei, T. Tao, and Y. Su, "Multiple-component polarimetric decomposition with new volume scattering models for Polsar urban areas," *IET Radar Sonar Navigat.*, vol. 11, no. 3, pp. 410–419, 2017.

[22] S. Quan, D. Xiang, B. Xiong, H. Canbin, and K. Gangyao, "A hierarchical extension of general four-component scattering power decomposition," *Remote Sens.*, vol. 9, no. 8, 2017, Art. no. 856.

[23] S. W. Chen, M. Ohki, M. Shimada, and M. Sato, "Deorientation effect investigation for model-based decomposition over oriented built-up areas," *IEEE Geosci. Remote Sens. Lett.*, vol. 10, no. 2, pp. 273–277, Mar. 2013.

[24] X. Sun, H. Song, R. Wang, and N. Li, "High-resolution polarimetric SAR image decomposition of urban areas based on a POA correction method," *Remote Sens. Lett.*, vol. 9, no. 4, pp. 363–372, 2018.

[25] L. Deng and Y. Yan, "Improving the Yamaguchi4 decomposition method using selective polarization orientation compensation," *Can. J. Remote Sens.*, vol. 42, no. 2, pp. 125–135, 2016.

[26] J.-S. Lee, D. L. Schuler, and T. L. Ainsworth, "Polarimetric SAR data compensation for terrain azimuth slope variation," *IEEE Trans. Geosci. Remote Sens.*, vol. 38, no. 5, pp. 2153–2163, Sep. 2000.

[27] J. Lee, T. L. Ainsworth, and Y. Wang, "Polarization orientation angle and polarimetric SAR scattering characteristics of steep terrain," *IEEE Trans. Geosci. Remote Sens.*, vol. 56, no. 12, pp. 7272–7281, Dec. 2018.

[28] H. Li, J. Chen, Q. Li, G. Wu, and J. Chen, "Mitigation of reflection symmetry assumption and negative power problems for the model-based decomposition," *IEEE Trans. Geosci. Remote Sens.*, vol. 54, no. 12, pp. 7261–7271, Dec. 2016.

[29] H. Li, Q. Li, G. Wu, J. Chen, and S. Liang, "The impacts of building orientation on polarimetric orientation angle estimation and model-based decomposition for multilook polarimetric SAR data in urban areas," *IEEE Trans. Geosci. Remote Sens.*, vol. 54, no. 9, pp. 5520–5532, Sep. 2016.

[30] A. Bhattacharya, G. Singh, S. Manickam, and Y. Yamaguchi, "An adaptive general four-component scattering power decomposition with unitary transformation of coherency matrix (AG4U)," *IEEE Geosci. Remote Sens. Lett.*, vol. 12, no. 10, pp. 2110–2114, Oct. 2015.

[31] D. Xiang, T. Tang, Y. Ban, Y. Su, and G. Kuang, "Unsupervised polarimetric SAR urban area classification based on model-based decomposition with cross scattering," *ISPRS J. Photogrammetry Remote Sens.*, vol. 116, pp. 86–100, 2016.

[32] S. R. Cloude and K. P. Papathanassiou, "Polarimetric SAR interferometry," *IEEE Geosci. Remote Sens. Lett.*, vol. 36, no. 5, pp. 1551–1565, Sep. 1998.

[33] S. Chen, X. Wang, Y. Li, and M. Sato, "Adaptive model-based polarimetric decomposition using PolInSAR coherence," *IEEE Trans. Geosci. Remote Sens.*, vol. 52, no. 3, pp. 1705–1718, Mar. 2014.

[34] Y. Wang, W. Yu, X. Liu, and C. Wang, "A hierarchical extended multiple-component scattering decomposition of polarimetric SAR interferometry," *IEEE Geosci. Remote Sens. Lett.*, vol. 17, no. 7, pp. 1193–1197, Jul. 2020.

[35] J. S. Lee, M. R. Grunes, T. Ainsworth, I. Hajnsek, T. Mette, and K. P. Papathanassiou, "Forest classification based on L-band polarimetric and inteferometric SAR data," *in Proc. Int. POLINSAR Workshop*, 2005, pp. 1–7.

[36] K. Kitayama, Y. Yamaguchi, J. Yang, and H. Yamada, "Compound scattering matrix of targets aligned in the range direction," *IEICE Trans. Commun.*, vol. E 84-B, no. 1, pp. 81–88, 2001.

[37] Y. Wang, W. Yu, C. Wang, and X. Liu, "A modified four-component decomposition method with refined volume scattering models," *IEEE J. Sel. Topics Appl. Earth Observ. Remote Sens.*, vol. 13, pp. 1946–1958, 2020.

[38] J. Yang, Y. N. Peng, and S. M. Lin, "Similarity between two scattering matrices," *Electron. Lett.*, vol. 37, no. 3, pp. 193–194, 2002.

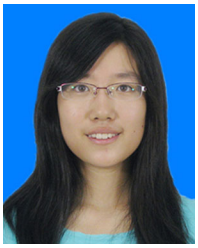

Yu Wang (Student Member, IEEE) was born in Shandong, China, in 1993. She received the B.S. degree in telecommunication engineering from Jilin University, Changchun, China, in 2016. She is currently working toward the Ph.D. degree in image classification and target decomposition technique for polarimetric synthetic aperture radar and polarimetric synthetic aperture radar interferometry from the University of Chinese Academy of Science, Beijing, China.

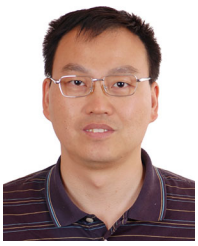

Weidong Yu (Member, IEEE) was born in Henan, China, in 1969. He received the M.Sc. and Ph.D. degrees in electrical engineering from the Nanjing University of Aeronautics and Aerospace, Nanjing, China, in 1994 and 1997, respectively.

Since 1997, he has been with the Institute of Electronics, Chinese Academy of Science, Beijing, China, where he became a Professor of Communication and Information Systems in 2000. He was the Chief Designer for several SAR systems. He is the Deputy Director of the Department of Space Microwave Remote Sensing System, Institute of Electronics, Chinese Academy of Sciences. He has authored more than 50 papers. He holds five patents. His current research interests include airborne and spaceborne synthetic aperture radar system design, and their signal processing.

Wentao Hou received the B.S. degree from Xidian University, Xi'an, China, in 2017. He is currently pursuing the Ph.D. degree with Space Microwave Remote Sensing System Department, Aerospace Information Research Institute, Chinese Academy of Sciences, Beijing, China.

He is currently with the University of Chinese Academy of Sciences, Beijing, China.His research interests include polarimetric/compact polarimetric SAR image processing and information extraction.